ACS NANO

www.acsnano.org

ARTICLE

Three-Dimensional Remodeling of SARS-CoV2-Infected Cells Revealed by Cryogenic Soft X-ray Tomography

Victoria Castro,[⊥] Ana Joaquina Pérez-Berna,[⊥] Gema Calvo, Eva Pereiro,* and Pablo Gastaminza*

Cite This: https://doi.org/10.1021/acsnano.3c07265

Read Online

ACCESS | Metrics & More | Article Recommendations | Supporting Information

ABSTRACT: Plus-strand RNA viruses are proficient at remodeling host cell membranes for optimal viral genome replication and the production of infectious progeny. These ultrastructural alterations result in the formation of viral membranous organelles and may be observed by different imaging techniques, providing nanometric resolution. Guided by confocal and electron microscopy, this study describes the generation of wide-field volumes using cryogenic soft-X-ray tomography (cryo-SXT) on SARS-CoV-2-infected human lung adenocarcinoma cells. Confocal microscopy showed accumulation of double-stranded RNA (dsRNA) and nucleocapsid (N) protein in compact perinuclear structures, preferentially found around centrosomes at late stages of the infection. Transmission electron microscopy (TEM) showed accumulation of membranous structures in the vicinity of the infected cell nucleus, forming a viral replication organelle containing characteristic double-membrane vesicles and virus-like particles within larger vesicular structures. Cryo-SXT revealed viral replication organelles very similar to those observed by TEM but indicated that the vesicular organelle observed in TEM sections is indeed a vesiculo-tubular network that is enlarged and elongated at late stages of the infection. Overall, our data provide additional insight into the molecular architecture of the SARS-CoV-2 replication organelle.

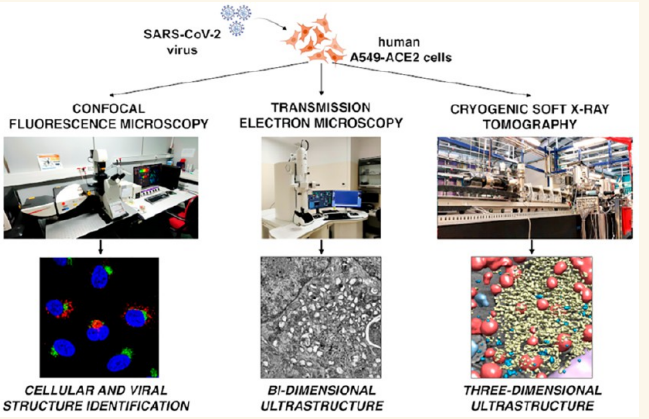

KEYWORDS: *SARS-CoV-2, microscopy, cryo-SXT, viral replication, vesiculo-tubular network*

With more than 770 million people infected and at least 6.9 million confirmed deaths, the current COVID-19 pandemic constitutes a global health problem with a major socioeconomic impact due to the direct burden on human health but also to different restriction measures, which caused a reduction of the circulation of people and goods worldwide. The virus causing the COVID-19 pandemic, SARS-CoV-2, is a coronavirus (family Coronaviridae, genus *Betacoronavirus*) genetically related to SARS-CoV-1, responsible for the severe acute respiratory syndrome (SARS) outbreak in the early 2000s.[1] Together with the middle east respiratory syndrome (MERS) virus, a highly pathogenic coronavirus, also from zoonotic origin, they constitute the three major human pathogenic coronaviruses.[2]

While coronaviruses differ in their tropism and pathogenicity, the viruses in this family share basic aspects of their replication cycle in the host cell.[3] The infection cycle is initiated by engagement of a host receptor by the spike (S) glycoprotein, which will mediate particle internalization and genome release after fusion of the viral and endosomal membrane.[4] Once the genome is released to the cytosol, it is translated to produce viral proteins in a first round of translation. Approximately two-thirds of the viral genome encode two open reading frames, ORF1a and ORF1b, which are processed mainly by viral proteases (nsp3 and nsp5) into 16 nonstructural proteins (nsp) devoted to the production and modification of viral RNAs. These include enzymatic activities such as viral RNA-dependent RNA polymerase and RNA-modifying enzymes as well as proofreading activities.[5] The viral RNA transcription and replication complex (RTC) is

Received: August 4, 2023
Revised: October 27, 2023
Accepted: October 27, 2023

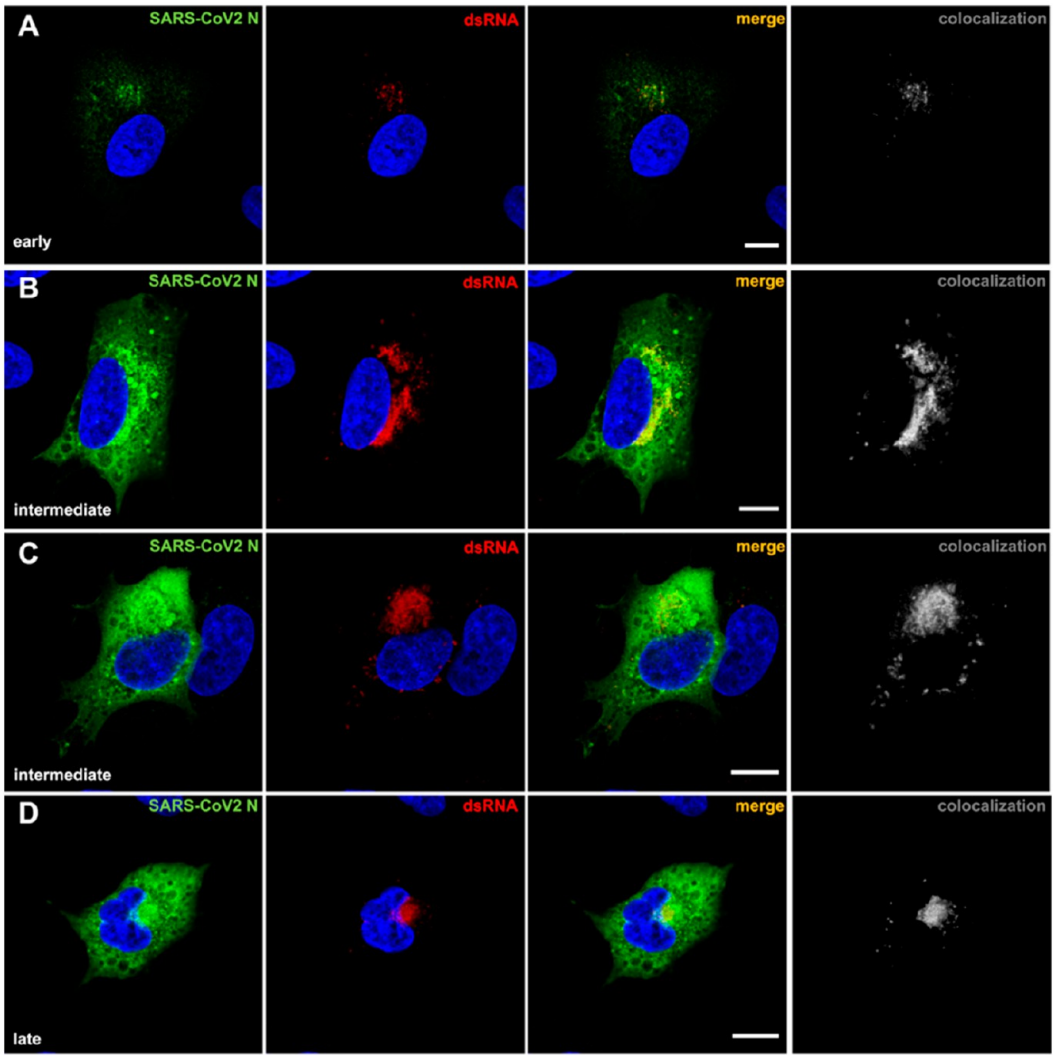

Figure 1. Different distributions of SARS-CoV-2 N protein and dsRNA in infected human lung adenocarcinoma cells at different stages of the infection. A549-ACE2 cells were inoculated with SARS-CoV-2 (MOI 0.01), incubated at 37 °C for 24 h, chemically fixed and processed for immunofluorescence microscopy using antibodies against dsRNA (red) and SARS-CoV-2 N protein (green). Nuclei were counterstained with DAPI (blue). Scale bars represent 10 μm. (A–D) Examples of cells with increasing amounts of dsRNA signal (red) indicating different stages of the infection: (A) early, (B, C) intermediate, and (D) late stages of infection.

responsible for the production of subgenomic, negative-strand RNAs (sgRNAs) by a unique mechanism involving a discontinuous transcription process.[6] These sgRNAs will serve as a template for the production of viral mRNA, which, in turn, will be translated to produce all the viral proteins, including the structural proteins (S, M, E, and N) and additional open reading frames (ORFs) encoding so-called "accessory" proteins, given that many are not strictly essential for virus propagation in cell culture.[7]

Expression of the viral proteins results in a profound remodeling of the infected cell cytoplasm, with the characteristic membranous compartment, generically denominated viral replication organelle (VRO).[8] One of the salient characteristics of the coronavirus VRO is the presence of double-membrane vesicles (DMVs), where various nsp and double-stranded RNA (dsRNA) have been shown to colocalize and where active RNA-dependent RNA synthesis has been shown to occur.[8−11] Thus, DMVs are the structures where coronavirus RNA replication is thought to occur.[8]

While the nature and origin of the membranes may differ, DMVs are also the putative RNA replication organelle for hepatitis C virus (HCV).[12,13] We have previously used cryogenic soft X-ray tomography (cryo-SXT) to characterize the context in which the HCV membranous compartment is formed and determined a spatial coincidence between HCV-induced membranous alterations with that of mitochondria showing ultrastructural signs of stress,[14] a hallmark of HCV infection and pathogenesis.[15]

In this study, we have taken advantage of sample characterization by confocal immunofluorescence microscopy and TEM, to acquire wide-field, nanometric-resolution three-dimensional maps of SARS-CoV-2-infected human cells (e.g. 30 nm half-pitch) by cryo-SXT. This technique is based on the differential absorption of X-rays by carbon, calcium, fluorine, nitrogen, hydrogen, and sulfur, their organic compounds, and oxygen atoms to resolve the cellular ultrastructure without the need for any contrast agent or sectioning.[16−21] Cryo-SXT shows a perinuclear membranous compartment containing vesicles with diameters compatible with those of DMVs, with

https://doi.org/10.1021/acsnano.3c07265
ACS Nano XXXX, XXX, XXX−XXX

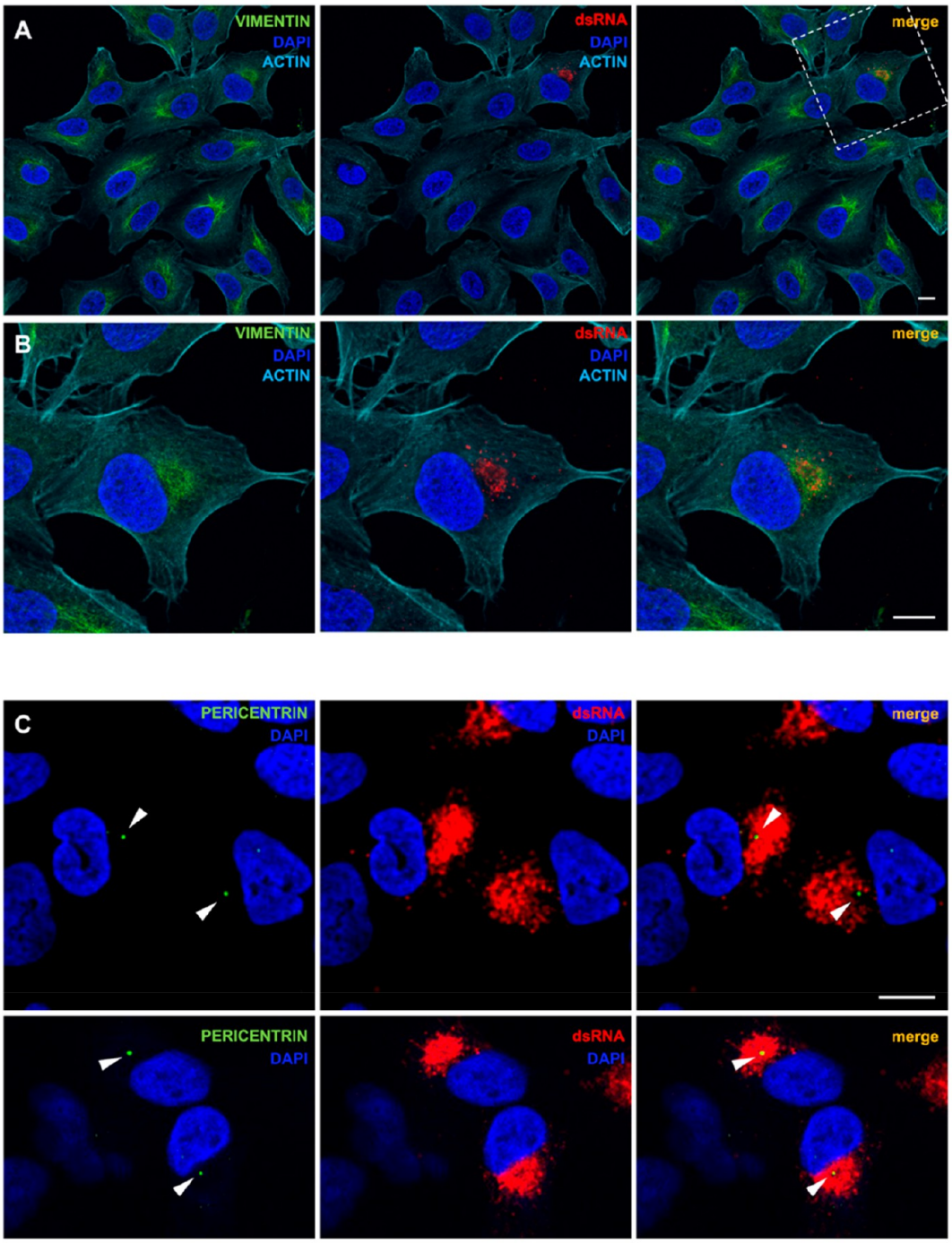

Figure 2. dsRNA-positive structures near centrosomes surrounded by vimentin during SARS-CoV-2 infection. A549-ACE2 cells were inoculated with SARS-CoV-2 (MOI 0.01), incubated at 37 °C for 24 h, chemically fixed, and processed for immunofluorescence microscopy using antibodies against dsRNA (red) and vimentin (A, B; green) or pericentrin (C; green). Nuclei and actin filaments were counterstained with DAPI (blue) and Alexa 660-conjugated phalloidin (A, B; cyan), respectively. (B) corresponds to a zoomed-in image of the indicated area in (A). Scale bars represent 10 μm.

surrounding smaller mitochondria displaying signs of stress. Moreover, tomograms collected from cells at late infection stages reveal the formation of larger and elongated vesicular structures. This 3D approach provides additional, quantifiable structural information which complements that obtained with 2D transmission electron microscopy in similar infection models, as discussed below.

RESULTS/DISCUSSION

To characterize the biological samples to be imaged using cryo-SXT, A549-ACE2 cells were plated onto glass coverslips and inoculated at low multiplicity of infection (MOI 0.01) to monitor viral antigen expression, subcellular localization, and potential changes in relevant cellular structures by confocal microscopy. In this experimental setting, multiple rounds of infection occur in this time frame. Thus, noninfected cells, cells

https://doi.org/10.1021/acsnano.3c07265
ACS Nano XXXX, XXX, XXX−XXX

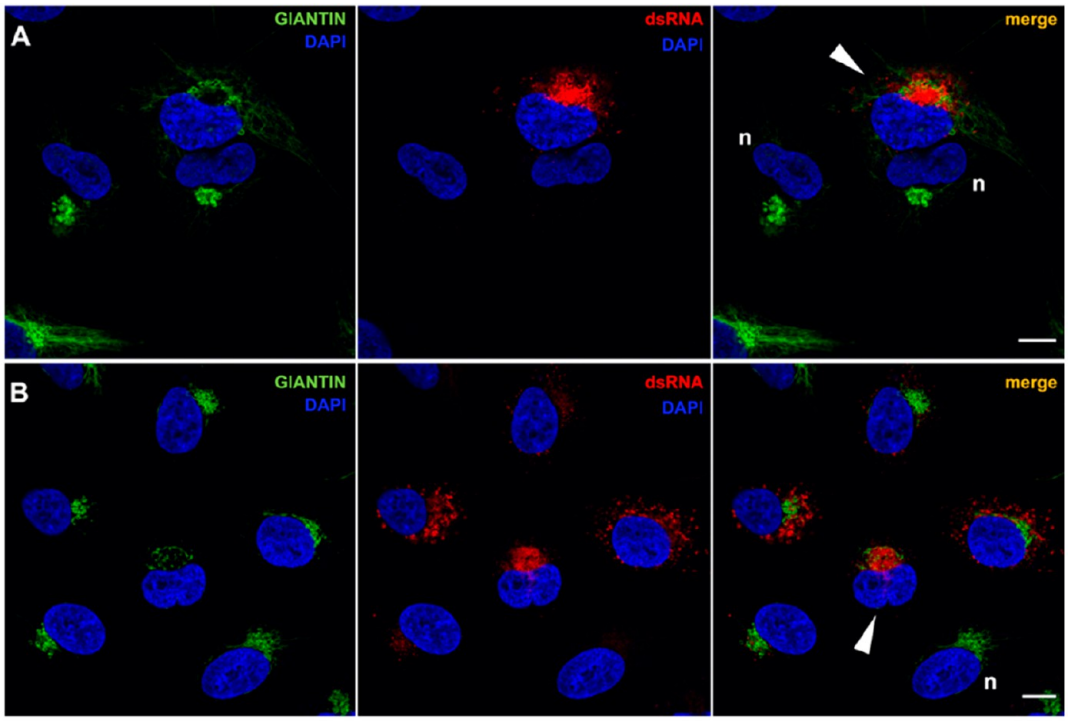

Figure 3. Golgi apparatus dispersion in SARS-CoV-2-infected cells. A549-ACE2 cells were inoculated with SARS-CoV-2 (MOI 0.01), incubated at 37 °C for 24 h, chemically fixed, and processed for immunofluorescence microscopy using antibodies against dsRNA (red) and Golgi marker giantin (green). (A) and (B) show two different representative fields of infected cells. Arrowheads show late stages of infection and (n) dsRNA-negative, noninfected cells. Nuclei were counterstained with DAPI (blue). Scale bars represent 10 μm.

infected with the input virus, and cells infected with progeny virus derived from the former will represent different stages of the viral infection in the same sample. This is convenient for imaging different stages of infection on the same sample support.

To identify infected cells at different stages of infection, primary antibodies recognizing dsRNA and SARS-CoV-2 N protein were used to prepare samples for confocal immunofluorescence microscopy. While both antibodies clearly labeled only infected cells, the expression pattern of these two antigens differed in their relative localization, depending on their expression levels. Based on the previous knowledge generated in similar experimental models, we have documented different stages of the infection based on the fact that the viral N protein and dsRNA fluorescent signal correlate with the time postinfection in single-cycle infection experiments.[11,22,23] Cells displaying low N protein and dsRNA signal, representing early stages of infection, showed a relatively diffuse pattern and discrete colocalizing puncta (Figure 1A). As the levels of N protein and dsRNA increase, representing intermediate stages of infection,[11,22] larger dsRNA puncta are observed colocalizing, at the confocal resolution, with N protein-positive structures that stand out from a diffuse N protein cytoplasmic staining (Figure 1B,C). Further increase in the dsRNA signal is associated with some degree of dsRNA-positive structure clustering, which partially colocalizes with N protein-positive structures (Figure 1B,C). It is noteworthy that not all N protein-positive discrete structures are dsRNA-positive. In fact, large N-positive vesicles excluding dsRNA staining are observed as dsRNA signal clusters close to the nucleus in cells expressing a high dsRNA signal (Figure 1C). Clustering of dsRNA structures results in a compact structure apposed to the cell nucleus in a manner that often suggests nuclear deformation at the contact area, as determined by DAPI staining (Figure 1D). As was previously shown,[11,22] cell cytoplasm starts to retract around the nucleus, loses the broad contacts with the substrate, and tends to round up at late stages of the infection (Figure 1D).

The perinuclear compact viral structure occurs in areas where intermediate filament elements such as vimentin also accumulate, as previously reported by Cortese et al.[11] In noninfected cells, vimentin forms a characteristic filamentous network in the perinuclear area (Figure 2A). As infection progresses, dsRNA staining tends to cluster in vimentin positive structures, which forms a sort of so-called "cage" in which the viral machinery appears to be constrained (Figure 2B Figure S1). Although cytoplasmic retraction at late stages of the infection may contribute to concentration of the viral machinery, formation of the compact juxtanuclear dsRNA and N protein structure precedes cytoplasmic shrinking, as shown by actin staining (Figure 2A,B and Figure S1). Vimentin cages have been associated with cell structures devoted to coping with stress situations by accumulating protein aggregates in so-called "aggresomes". These structures do not have an external membrane and are delimited by intermediate filaments in pericentriolar areas of the cell.[24] Moreover, an analysis of infected cells suggests that a pericentrin-positive spot is frequently observed within the area where most dsRNA signal accumulates at late stages of the infection, although no colocalization was observed between pericentrin and dsRNA signals (Figure 2C). Together with the vimentin cage around dsRNA staining, viral replication organelles (VROs) appear to be contained in an area of the cytosol that has characteristics similar to those of aggresomes.[24]

A striking difference between infected and noninfected cells is the Golgi apparatus morphology. Noninfected cells show a

https://doi.org/10.1021/acsnano.3c07265
ACS Nano XXXX, XXX, XXX−XXX

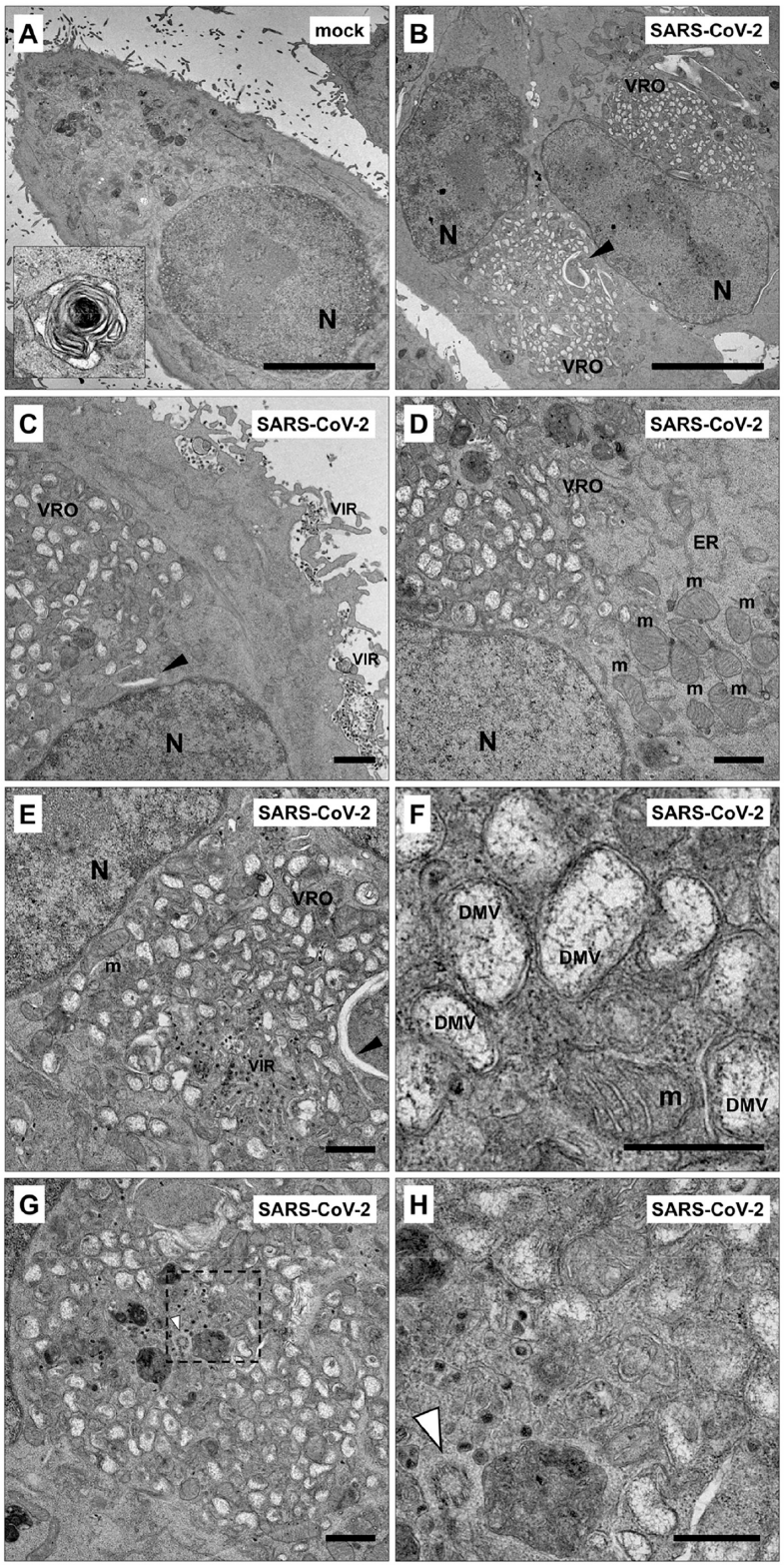

Figure 4. Transmission electron microscopy of SARS-CoV2-infected human cells. A549-ACE2 cells were inoculated at MOI 3 and incubated for 20 h before chemical fixation and processing for TEM. Representative images of (A) mock infected cells, where the inset shows the ultrastructure of a multilamellar body (MLB), and (B−F) SARS-CoV-2-infected cells. Definitions: N, nucleus; VRO, viral replication organelle; m, mitochondrion; VIR, putative virions; DMV, double-membrane vesicle; black arrowheads, enlarged ER cisternae; white arrowheads, centriole. Scale bars: (A, B) 5 μm; (C−E) 1 μm; (F) 0.5 μm. The scale bar in the inset to (A) is 1 μm. (H) corresponds to the area delimited by a dashed line in (G).

relatively compact and localized Golgi structure, as shown by giantin staining (Figure 3A,B; n denotes noninfected). However, cells at late stages of infection, i.e., with strong and compact perinuclear dsRNA staining, show strong alterations

https://doi.org/10.1021/acsnano.3c07265
ACS Nano XXXX, XXX, XXX−XXX

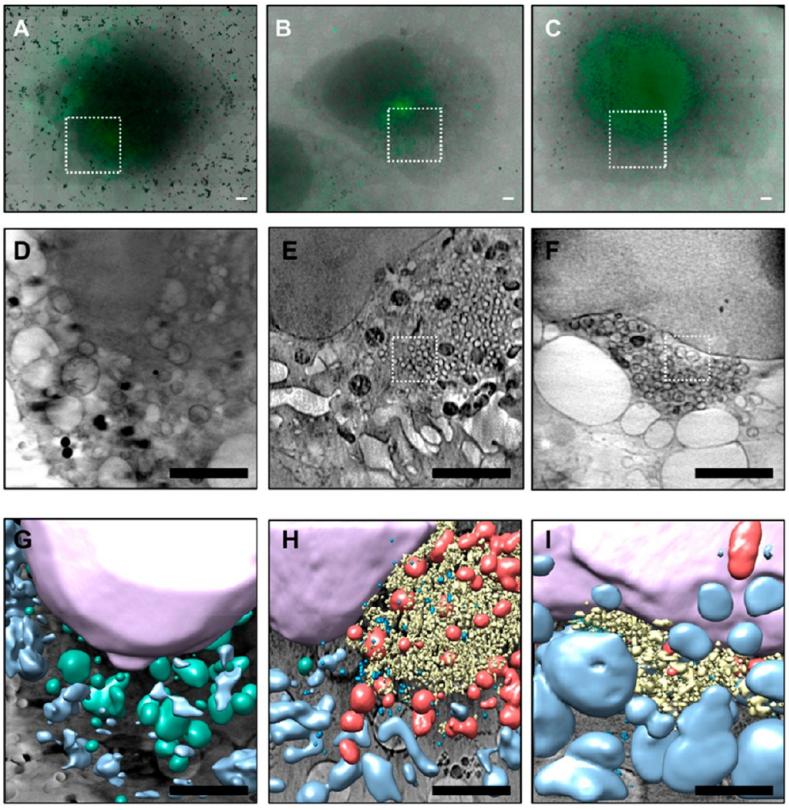

Figure 5. Three-dimensional reconstruction of control, intermediate, and late SARS-CoV2-infected cells by cryo-SXT: control, noninfected cells (A, D, G) and intermediate (B, E, H) and late SARS-CoV-2 infection stages (C, F, I). Green cryo-epifluorescence signal of the infection stage reporter (A−C). Tile-scanned projections of selected cells showing cryo-SXT areas acquired (square; D−F) as well as volume slices of the tomograms from the boxed areas (G−I) are shown. Color-coded manual segmentation of the surface boundaries identifying different organelles (nuclei, purple; large cytoplasmic vesicles, light blue; mitochondria, green; abnormal mitochondria, red; vesicular network, yellow; virion-like structures, dark blue) is presented in the control and infected cells (G−I). Scale bars: (A−C) 2 μm; (D−I) 1 μm.

in Golgi morphology (Figure 3A,B; arrowheads). These alterations include Golgi fragmentation and even dispersion of the vesicular Golgi network as previously reported.[11]

To gain insight into the ultrastructural alterations induced by SARS-CoV-2, A549-ACE2 cells were inoculated at MOI 3, to achieve a high percentage of infected cells, and incubated for 20 h, a time sufficient to observe fully formed viral structures.[9,11] At this time, infected cells and noninfected controls were processed for transmission electron microscopy (TEM). Uninfected A549-ACE2 showed the expected ultrastructure with well-defined organelles, including multilamellar bodies (MLBs) (Figure 4A, inset), a structure associated with surfactant production in type II alveolar cells.[25] In contrast, MLBs in SARS-CoV-2 infected cells were scarce, while prominent ultrastructural alterations in the form of a compact, well-delimited vesicular compartment (Figure 4B−F) were readily observed at low magnification. Double-membrane vesicles (DMVs) 250−300 nm in diameter were clearly visualized within these large areas (Figure 4F; DMV), similar to those previously described for SARS-CoV-2 and other coronaviruses,[8,10,11] although some enlarged endoplasmic reticulum (ER) cisternae could also be observed (Figure 4B,C,E; black arrowheads). Mitochondria are less frequently observed in these areas and appear smaller and tightly packed within the VROs (Figure 4F; m). Outside these highly modified areas, mitochondria and endoplasmic reticulum cisternae show a relatively normal appearance, (Figure 4D; m). Discrete particles compatible in size and morphology with assembled virions were observed at the infected cell surface of the cytoplasm membrane (Figure 4C; VIR) and within VROs, in areas devoid of DMV clusters (Figure 4E; VIR). Some of the TEM images also revealed the presence of centrioles (Figure 4G,H; white arrowheads) within the perinuclear areas where VROs accumulate, consistent with the pericentrin staining shown above by confocal microscopy (Figure 2C). Overall, confocal microscopy and TEM data suggest marked alterations of the cellular ultrastructure but only provide two-dimensional information. Thus, we set out to gather three-dimensional information on whole cells to better understand SARS-CoV-2 infection-induced structural alterations using cryo-SXT.

To readily identify SARS-CoV-2 infected cells *in vivo*, without the need for immunostaining, A549-ACE2 cells were transduced with a retroviral construct expressing a reporter fluorescent construct susceptible to cleavage by the SARS-CoV-2 main protease (Mpro). Upon SARS-CoV-2 infection and Mpro expression, a construct EGFP signal is translocated from the ER to the nucleus of the infected cell, enabling identification of infected cells using live microscopy.[23] Reporter A549-ACE2 cells were seeded onto grids, inoculated at a low multiplicity of infection (MOI 0.01), and incubated for 24 h. As mentioned above for confocal microscopy studies, in multiple cycle infection (MOI 0.01), different stages of the infection are recapitulated in the different cells within the same sample grid and the use of prior knowledge on the temporal distribution of the fluorescent infection reporter[11,23] facilitates identifying cells at intermediate and late stages of the infection.

https://doi.org/10.1021/acsnano.3c07265
ACS Nano XXXX, XXX, XXX−XXX

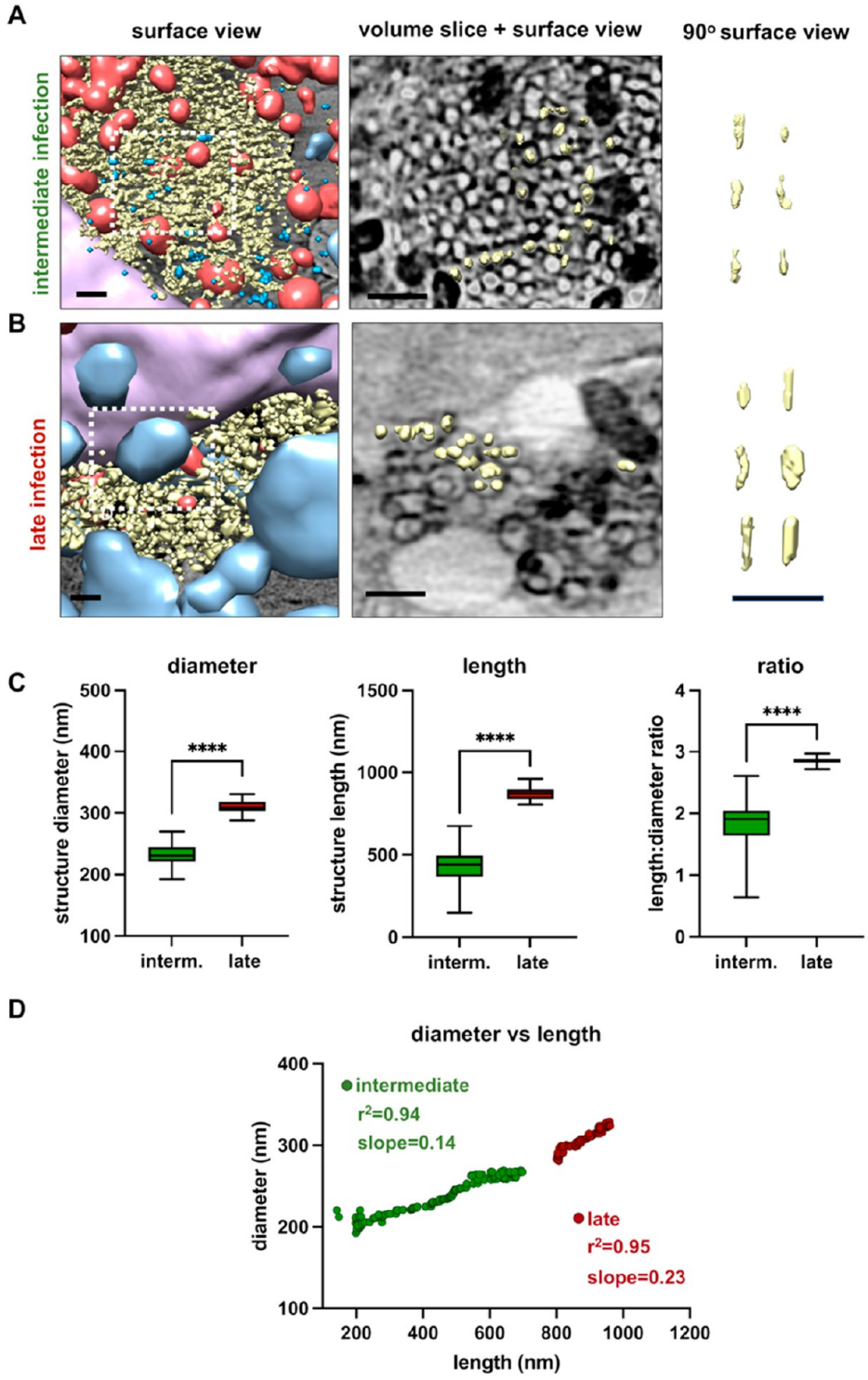

Figure 6. SARS-CoV-2 infection induces ultrastructural alterations of the intracellular membrane network. (A, B) Representative areas of intermediate (A) and late stages (B) of infection showing different alterations of the virus-induced membranous network by manual segmentation of the vesiculo-tubular structures (A, B surface view; left panels), volume slices showing segmentation of selected membranous structures (A, B volume slices + surface view; central panels), and 90° rotation of segmented structures of the in-depth tubular network (A B surface view, right panels). Scale bars: 1 μm. (C) Measurements of the virus-induced structures showing diameter (left), length (central) and length:diameter ratio (right) at intermediate and late stages of infection (N = 496; 5 tomograms each). Data in (C) are shown as a box plot displaying the upper quartile, median, and lower quartile as well as whiskers showing highest and lowest values. Statistical significance between the average of the groups was calculated using a two-tailed Mann−Whitney U test. (D) Representation of individual structure length versus diameter expressed in nm. Simple linear regression was individually calculated for intermediate and late infection stage data sets. r^2 as well as the adjusted line slope are shown (N = 496; 5 tomograms each data set). The segmentation color code is identical with that in Figure 5.

https://doi.org/10.1021/acsnano.3c07265
ACS Nano XXXX, XXX, XXX−XXX

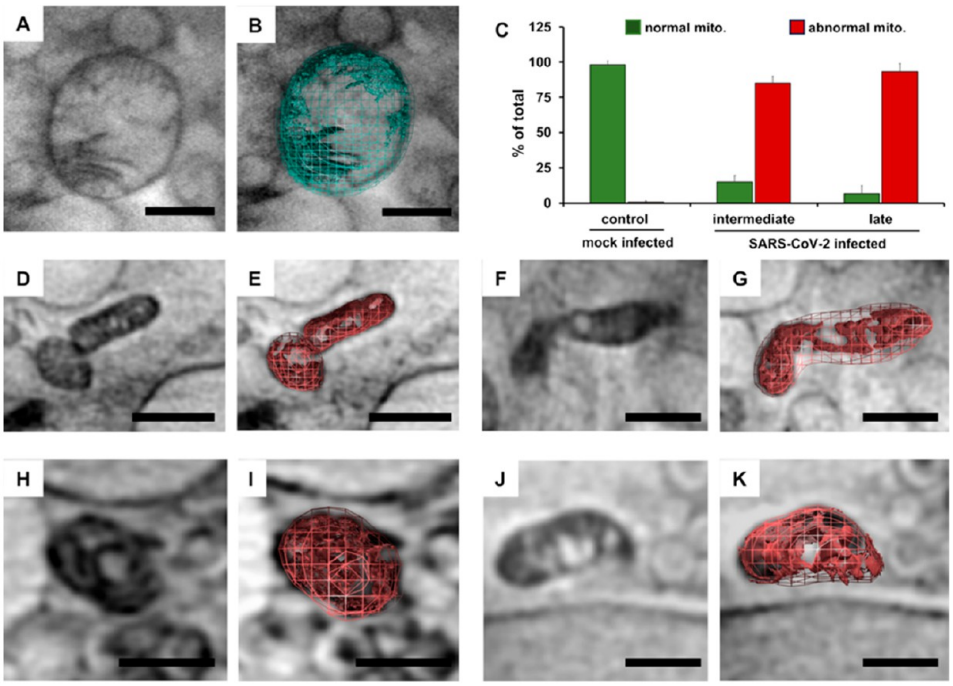

Figure 7. Mitochondria in control and SARS-CoV-2-infected cells. Comparative analysis of the mitochondrial morphology of control (A, B) and SARS-CoV-2-infected cells at intermediate (D−G) and late stages (H−K) of infection. Mitochondrial morphology and absorption contrast were used as criteria for classification into normal or abnormal categories (see Methods/Experiments). (C) Relative frequency of normal versus abnormal mitochondria quantified for control and intermediate and late infection stages (N = 2241 from 15 tomograms each). Volume slices (A, D, F, H, J) and manually segmented surface representations (B, E, G, I, K). Scale bars: 0.5 μm.

To comply with biosafety regulations, the cryo-SXT samples were chemically fixed. Grids were first imaged by cryo-epifluorescence microscopy to identify infected cells primarily by subcellular localization of the corresponding fluorescent signal (Figure 5A−C and Figure S2). Once the regions of interest had been identified, grids were transferred in cryogenic conditions to the Mistral beamline[26] for data acquisition followed by tomogram reconstruction.

Noninfected cells displayed fluorescent signal exclusively in the cytosol (Figure 5A and Figure S2) and showed a typical ultrastructure, with readily identifiable organelles,[27] such as nucleus and mitochondria displaying low absorbing lumen and visible cristae, as well as different vesicular organelles, including low absorbing vacuoles near the plasma membrane (Figure 5D,G, Figure 7A, andMovie S1). Real-time monitorization of SARS-CoV-2 infection in A549-ACE2 cells expressing the aforementioned reporter has been described using real-time fluorescence videomicroscopy.[11,23] In those studies, nuclear translocation of the fluorescent reporter starts predominantly 7−9 h postinoculation and reflects an intermediate−late stage of the infection.[11,23] Late stages of the infection are characterized by a full nuclearization of the reporter and a tendency for the cells to display cytoplasmic retraction, nuclear deformation, and subsequent death.[11,23] Taking advantage of the fluorescent signal as a temporal marker of the infection, we can assume that a partial nuclear fluorescent signal represents an intermediate stage of infection (Figure 5B), preceding total nuclearization of the fluorescence, which occurs at late stages of infection (Figure 5C). Quantitative analysis of the cryo-SXT volumes was performed on five infected cells at an intermediate infection stage (Figure 5B,E,H) and five at a late stage (Figure 5C,F,I). Data collected from cells at intermediate stages of infection revealed the presence of clusters of medium-sized vesicles (Figure 5E, H, Figure 6A, andMovie S2) in the perinuclear area within the cytoplasm at intermediate stages. These tightly packed tubular vesicles close to the cell nucleus display a rather uniform diameter of around 233 ± 18 nm and lengths of 432 ± 129 nm in the intermediate infection data set (p < 0.05, N = 496, five cells) (Figure 6C). Given their size, location, and reduced lumen absorption, these structures likely correspond to viral replication compartments characterized by the presence of DMVs (Figure 4F) and enlarged ER tubules (Figure 5E,H) similar to those previously observed in other cell culture models.[10,11,28]

Cells displaying full EGFP marker nuclearization and prominent cytoplasmic retraction, reporting late infection stages[11,23] (Figure 5C), show similar clusters of vesicles in the perinuclear region, although with a visible absorbing internal content (Figure 5F, I andFigure 6D−F). An infection-induced vesicular network is apposed to the nuclear envelope, leading to local nuclear deformation (Figure 5, Figure 6B, and Movie S3), a feature reminiscent of the observations made with dsRNA and DAPI staining by confocal immunomicroscopy (Figure 1D). The juxtanuclear vesicles are more uniform and significantly larger in diameter (306 ± 10 nm; p < 0.05, N = 496) at late stages of infection as compared to the intermediate infection stages. They may correspond to “vesicle packets”, that have been described previously by TEM and cryo-EM[9−11] and defined as juxtaposed DMVs undergoing homotypic fusion events (Figure 6B). Remarkably, these structures are significantly longer (875 ± 43 nm; p < 0.05, N = 496) than those observed at earlier stages of infection (Figure 6C). The vesicular structures have a length proportional to their diameter at both intermediate and late stages of infection (Figure 6D). However, their length-to-diameter ratio is greater at the late infection stage (2.856 ± 0.054 in late vs 1.825 ±

https://doi.org/10.1021/acsnano.3c07265
ACS Nano XXXX, XXX, XXX−XXX

0.42 in intermediate stages; $p < 0.05$, $N = 496$) (Figure 6C). Finally, structures resembling viral particles were identified at intermediate infection stages due to their size and subcellular location (Figure 5D,H and Figure 6A, dark blue). In any case, tomographic reconstruction of whole cell regions demonstrates that the perinuclear vesiculo-tubular network constitutes the most prominent virus-induced cellular reorganization in SARS-CoV2-infected cells at intermediate and late stages of infection (Figure 6A,B).

Concomitant with the perinuclear cluster of vesicles, abnormal mitochondria, as defined below, are visualized (Figure 5H,I; red). Control cells present a large number of heterogeneous and pleomorphic mitochondria with recognizable cristae (Figure 7A,B) and a low-absorbing matrix, comparable to the overall cytoplasm. SARS-CoV-2-infected cells, though, display abnormal mitochondria with enlarged cristae and increased absorption contrast, suggesting matrix condensation (Figure 7D−K), both of which are hallmarks of mitochondrial dysfunction.[29] Mitochondrial morphological alterations were quantified in 15 different cells for each condition (Figure 7C). In control cells, 98% ($N = 698$) of the mitochondria display a normal structure, while in the intermediate infection stage, 85% ($N = 967$, Figure 7C) of the mitochondria presented an abnormal ultrastructure (Figure 7D−G). This effect was even more prominent in cells at the late infection stage, for which 93% ($N = 796$, Figure 7C) of mitochondria presented abnormal structures (Figure 7H,K). Interestingly, normal mitochondria are also visualized in adjacent areas devoid of infection alterations (Figures 4D and Figure 5H, green). Mendonça et al.[28] as well as Cortese et al.[11] also communicated smaller, dysfunctional mitochondria as compared to their counterparts in uninfected cells. This strongly suggests that SARS-CoV-2 infection causes mitochondrial dysfunction in the host cell.[30] A similar phenomenon was already reported for HCV-infected cells using cryo-SXT.[14]

Cryo-SXT has allowed visualizing major ultrastructural alterations induced by SARS-CoV-2 infection in human lung adenocarcinoma cells at nanometric spatial resolution (27.7 nm half pitch resolution; see Figure S3). This technique provides an intermediate resolution approach bridging visible light fluorescence and electron microscopy and requires minimal sample preparation, i.e., vitrification in aqueous buffer, in contrast with other higher resolution techniques that may require chemical modification and/or sample sectioning.[21] Nevertheless, herein, chemical fixation was required as a biosafety measure to inactivate infectious viruses and not for technical reasons.

Quantitation of cryo-SXT volumes of SARS-CoV-2-infected cells reveals a network of clearly defined perinuclear vesicles and tubules (Figures 5 and 6 and Movies S1−S3). The diameter of the perinuclear structures shown herein are very consistent with previous information gathered by cryo-ET by others.[10,11] However, although cryo-ET provides excellent resolution and molecular detail, the technique is limited to thin cryosections; thus, no information on the length of the virus-induced tubular structures has been previously reported. In this study, cryo-SXT analyses show a statistically significant increase in diameter, length, and length-to-diameter ratio at late infection stages, where elongated perinuclear tubules show additional intraluminal contents, as compared with the vesicular structures found at earlier stages of infection (Figure 6).

Confocal microscopy images show that dsRNA-positive discrete puncta tend to collapse into larger perinuclear structures as the dsRNA signal increases in a given cell at intermediate−late stages of the infection (Figure 1). Interestingly, very compact dsRNA-positive structures surrounded by a vimentin "cage" are observed close to the nucleus in such an intimate connection that some nuclei appear to be deformed by dsRNA-positive structures at late stages of the infection (Figure 1D). Thus, it is likely that the vesicular perinuclear network observed in SARS-CoV-2-infected cells represents areas where dsRNA and N protein accumulate along the infection. It has been proposed that coronavirus-infection-related dsRNA, i.e., viral replication intermediates, are generated within DMVs, and high-resolution cryo-electron tomograms suggest the presence of viral RNA in the lumen of these structures.[10] Similar to other coronaviruses (MERS),[8,10] DMVs observed in SARS-CoV-2-infected cells show a heterogeneous diameter of around 300 nm in different cell lines.[9−11] However, temporal resolution of these structures revealed that DMVs are smaller, around 185 nm at early stages of the infection, and that larger vesicles are observed at later stages, around 300 nm.[11] Interestingly, several authors using TEM, cryo-ET or cryo-SXT described that larger DMVs included several internal vesicles within a unique external membrane[8,10,11] which may derive from the fusion of the external membrane of several DMVs.[10] Remarkably, cryo-SXT tomograms of cells at intermediate stages of the infection enabled visualization of tubular vesicles with a low-contrast lumen devoid of any visible content and with an average diameter of 230 nm, within the size range of intermediate infection events. In contrast, in tomograms collected from later stages of infection, where the cell is clearly colonized by the viral machinery and nuclear deformation by the presence of the vesiculo-tubular network is verified, viral structures show a larger diameter of around 300 nm and additional content in the lumen, a configuration that is reminiscent of the multivesicular DMVs or vesicle packets, as designated by Klein at al. for SARS-CoV-2-associated structures.[10] While there is wide agreement in the involvement in viral RNA replication of "canonical" DMVs, i.e., one internal membrane and one external membrane per vesicle, little is known on the function of "fused-DMVs" or vesicle packets in the coronavirus replication cycle. The presence of assembled virions in these vesicle packets has prompted the hypothesis that they could constitute budding surfaces as a sort of recycled membrane from former replication compartments.[10] In any case, late-stage vesicle packets could also constitute byproducts of the viral machinery that have no specific role in the infection cycle. Similarly, at late stages of HCV infection, DMVs are elongated and were designated as double-membrane tubules (DMTs).[12] These structures were designated as potential precursors of multiple-membrane vesicles (MMVs), a ultrastructural feature associated with very late HCV infection events of unknown function.[12]

The current resolution of our tomograms is at the limit to define whether the virus-like particles observed around and within the membranous network induced by SARS-CoV-2 are actual virions and preclude providing additional insight into this matter. Future studies, including correlative cryo-3D structured illumination microscopy and cryo-SXT (CLXT)[31] as well as improved isotropic resolution using dual tilt cryo-SXT,[32] may unambiguously identify these structures as virions, although high-resolution 3D maps of SARS-CoV-2 virions

https://doi.org/10.1021/acsnano.3c07265
ACS Nano XXXX, XXX, XXX−XXX

have been obtained by in situ cryo-ET.[10] In addition to the intrinsic resolution limitation of the optical SXT system, our reconstructed tomograms are affected by a "missing wedge", with the concomitant elongation artifact that needs to be corrected when determining the sizes of specific features (see Methods/Experiments). This angular limitation is due to the use of grids in which adherent cells are grown and imaged. Although this may be circumvented by the use of capillaries to allow full-rotation tomography, as reported by Loconte et al.,[19] it would entail enzymatic treatment of the cells, cell detachment, and confinement into a capillary which may disturb 3D cellular organization.

Regardless of these considerations, and in agreement with previous studies in similar systems,[11] it is clear that a SARS-CoV-2 replication organelle tends to concentrate in a structure that is delimited by a "cage" of intermediate filaments, such as vimentin. Being such an instrumental component of cell cytoskeleton, vimentin has been shown to intervene in several aspects of many viruses and also interacts with many different viral proteins.[33] Interestingly, confocal as well as TEM investigation shows the presence of pericentrin and centrioles in areas where dsRNA and DMVs accumulate, a characteristic shared by aggresomes.[24] Restriction of viral factories within these "cages" was previously demonstrated for large DNA viruses.[34] Cortese et al. reported similar vimentin cages in Zika virus infected cells,[35] and this structure has been proposed as a structural organizer that facilitates viral replication, at least for Zika and influenza viruses.[36,37] While the precise functional relevance of this structure remains unclear in SARS-CoV-2 infection, vimentin filaments have been proposed as physical barriers that limit intracellular vesicular trafficking, which may benefit the concentration of viral components in specific cytoplasmic locations to contribute to coordinating viral RNA replication and virion assembly. Vimentin cages may also be observed as essential components of cellular structures devoted to protein quality control, originally designated as "aggresomes" (reviewed in ref 38). Aggresomes are associated with different stress situations, where misfolded proteins may accumulate and are spatially compartmentalized in juxtanuclear, "membrane-free, cytoplasmic inclusion containing misfolded, ubiquitinated protein ensheathed in a cage of intermediate filaments".[24] As the knowledge on the mechanisms and the molecular determinants in the formation of these structure increases, novel denominations and important functional implications emerge for these spatially defined, vimentin-limited protein quality control structures.[38−40] Interestingly, it has been observed that formation of vimentin-positive structures involved in misfolded protein disposal may cause nuclear deformation, similar to what was observed at late stages of SARS-CoV-2 infection.[39,40]

Given the profound stress that SARS-CoV-2-infected cells undergo, it is possible that vimentin-delimited compartments are formed as means to isolating what the host cell identifies as misfolded proteins, resulting in concentration and isolation of the viral structures for optimal RNA replication and virion assembly while isolating viral machinery as a mechanism of innate immunity evasion. Regardless of these general considerations, a functional aggresome structure is required for efficient infection by different RNA viruses,[36] reinforcing the notion for a potential functional role of this structure in SARS-CoV-2 infection.

CONCLUSIONS

Overall, regardless of the functional considerations, our cryo-SXT data provide an additional piece of the puzzle in building a precise map of the ultrastructure of SARS-CoV-2-infected cells by providing insight into the overall structure of the viral replication organelle and the cellular context within which these changes occur.

METHODS/EXPERIMENTS

Cells. A549 expressing hACE2 (A549-ACE2) was generated by transduction of parental A549 cells (ATCC CRM-CCL-185) with a retroviral vector expressing human ACE2 and a selection marker that confers resistance to blasticidin. pCMV3-hACE2 was obtained from Sino Biologicals S.L. (Beijing, China). Reporter A549-ACE2 was generated by transduction with a lentiviral construct kindly provided by Dr. Cortese[23] from the Bartenschlager laboratory (University of Heidelberg), selection by supplementation of the culture media with puromycin (1 μg/mL), and sorting of the GFP-positive population by FACS. Vero-E6 cells (ATCC CRL-1586) were obtained from the Coronavirus laboratory (CNB-CSIC).

Cell cultures were maintained in DMEM supplemented with 10 mM HEPES, 1X nonessential amino acids (GIBCO), 100 U/mL penicillin−streptomycin (GIBCO), and 10% fetal bovine serum (FBS; heat-inactivated at 56 °C for 30 min). All infection experiments were performed at 37 °C in a CO_2 incubator (5% CO_2) in the presence of 2% FBS and in the absence of selection antibiotics.

SARS-CoV-2 Infection Experiments. SARS-CoV-2 (Coronaviridae; Orthocoronavirinae; *Betacoronavirus*; *Sarbecovirus*; strain NL/2020) was kindly provided by Dr. R. Molenkamp, Erasmus University Medical Center Rotterdam, and was propagated in Vero-E6 cells as previously described.[41] Virus stocks were titrated using tissue culture infectious dose 50 per mL ($TCID_{50}$/mL) determination[42] in Vero-E6 cells and using immunofluorescence microscopy using an antibody against SARS-CoV-2 N protein (Genetex HL344) by end-point dilution and infection foci counting in A549-ACE2 cells.[41]

Target A549-ACE2 cells were cultured in a BSL2 laboratory and were transferred to the BSL3 laboratory for inoculation with SARS-CoV-2 stocks. Specifically, virus stocks were diluted in DMEM supplemented with 2% FBS according to the desired virus concentration to achieve the indicated multiplicities of infection. After the designated incubation period, cell supernatants were carefully removed with a micropipet and disposable filter tips. Samples were subsequently submerged in chemical fixatives (2% paraformaldehyde-PBS for confocal microscopy and cryo-SXT or 1% tannic acid, 2.5% glutaraldehyde (TAAB) in 0.4 M HEPES buffer pH7.2 for TEM). After primary inactivation, cells were thoroughly washed with PBS. Primary chemical inactivation was ensured by using volumes of chemical fixative exceeding the virus inoculation volume and verified by determination of the intracellular infectivity titer of total cell lysates of parallel samples. These treatments are sufficient to completely inactivate intra- and extracellular infectious virus (<2 $TCID_{50}$/ml), as determined by titration of whole cell lysates and compared with nonfixed samples (>10^6 $TCID_{50}$/ml). Proper chemical fixation was also verified, as cellular integrity was completely maintained despite the use of detergents in the preparation of the cells via immunofluorescence microscopy. All residues, including micropipet tips, were submerged in Virkon in the safety cabinet. External surfaces of the cell culture plates were cleaned with Virkon and extracted from the safety cabinet in a secondary container, which was also cleaned with disinfectant. For complete sterilization of all surfaces before extraction from the BSL3 facility, a compulsory step to comply with biosafety regulations, primary and secondary containers were chemically treated in a pass-through box by microdiffusion/nebulization of peracetic acid and hydrogen peroxide solutions. All infection procedures were carried out in a certified BSL3 facility at the CNB-CSIC following the Spanish and European regulations. All activities were approved by the CNB Biosafety Committee, CSIC Ethics Committee, and the Spanish Ministry for the Ecological

https://doi.org/10.1021/acsnano.3c07265
ACS Nano XXXX, XXX, XXX−XXX

Transition and the Demographic Challenge and have been carried out by trained, fully equipped personnel.

Immunofluorescence Confocal Microscopy. A549-ACE2 cells were grown on glass coverslips and infected at a low multiplicity (MOI 0.01) with SARS-CoV-2. Multiple cycle infection (low multiplicity) was chosen to enable recapitulation of different stages of the infection in the same sample, using dsRNA staining levels as a surrogate for the stage of infection, based on previous studies in similar systems.[11,22] 24 h postinfection cells were fixed for 10 min at room temperature (RT) with a 2% EM-grade paraformaldehyde solution in PBS, washed twice with PBS, and incubated with an incubation buffer (3% BSA; 0.3% Triton X100 in PBS) for 1 h. All antibodies were diluted in incubation buffer: mouse anti-dsRNA (J2; Scicons), rabbit anti-SARS-CoV2 N (Genetex HL344), rabbit antigiantin (BioLegend 924302), rabbit antipericentrin (Abcam polyclonal ab4448), and rabbit antivimentin (Abcam ab188499). Primary antibodies were incubated with the cells for 1 h, after which the cells were washed with PBS and subsequently incubated with a 1:500 dilution of a goat antirabbit conjugated to Alexa 488 or goat antimouse Alexa 594 (Invitrogen-Carlsbad, CA). Nuclei or actin were stained with DAPI (Life Technologies) or Alexa 660 conjugated phalloidin (ThermoFisher) during the secondary antibody incubation using the manufacturer's recommendations. Cells were washed with PBS and mounted on glass slides with Prolong (Invitrogen-Carlsbad, CA).

Confocal microscopy was performed with a Leica TCS SP8 laser scanning system (Leica Microsystems). Images of 1024 × 1024 pixels at 8-bit grayscale depth were acquired sequentially every 0.13−0.3 μm through a 63×/1.40 N.A. immersion oil lens, employing LAS AF v 2.6.0 software (Leica Microsystems). Merged images were generated using Fiji software.[43]

Transmission Electron Microscopy. A549-ACE2 cells were seeded onto glass coverslips. Single-cycle infection (high MOI) was chosen to obtain a nearly 100% infection rate to readily identify viral structures 20 h postinfection. Thus, the day after, cells were inoculated with SARS-CV-2 at MOI 3 and fixed *in situ* 20 h postinfection with a mixture of 1% tannic acid and 2.5% glutaraldehyde (TAAB) in 0.4 M HEPES buffer pH 7.2 for 2 h at room temperature. Subsequently, fixative was removed and cells were kept in PBS. Before staining, cells were washed three times for 10 min with 0.4 M HEPES buffer pH 7.2 at 4 °C and stained with 1% osmium tetroxide in 0.8% potassium ferrocyanide (45 min; 4 °C), followed by three washing steps at 4 °C for 15 min with EM-grade water. Samples were then treated with 1% uranyl acetate in water (40 min; 4 °C) and washed three times with water as described above. Samples were dehydrated using solutions with increasing ethanol absolute dry (PANREAC) content (50, 75, and 90%) for 15 min each and two additional 30 min incubations with 100% ethanol at RT. Cultures were embedded in 50% epoxy resin 812 (TAAB) in ethanol for 3 h at RT, time after which the mixture was removed and replaced with the epoxy resin for an overnight incubation at RT. Resin was then removed and replaced with a epoxy resin preparation for an additional 5 h at RT. Samples were polymerized by incubation in a dry oven (60 °C, 48 h). Resin blocks were detached from coverslips by successive dipping into liquid nitrogen and hot water. Blocks were trimmed, and 70 nm thick sections were cut in parallel to the monolayer. Sections were subsequently transferred to Formvar-coated EM buttonhole grids and stained with aqueous uranyl acetate (10 min) and lead citrate (3 min). Sections were visualized on a JEOL 1400 flash electron microscope. Images were processed using Fiji software[43] to modify brightness and contrast.

Cryo-Soft X-ray Tomography. A549-ACE2 reporter cells were seeded onto gold quantifoil R 2/2 holey carbon-film microscopy grids (Au-G200F1) and inoculated the day after with SARS-CoV-2 (MOI 0.01). Multiple-cycle infections (low multiplicity) were chosen to enable recapitulation of different stages of the infection in the same sample. 24 h later, infection efficiency was verified by observation of nuclearization of the fluorescent infection reporter using an inverted epifluorescence microscope ZOE Cell Imager (20×/0.4 N.A.) at room temperature (Figure S2). Cells were subsequently fixed with 2% EM-grade PFA−PBS solution for 10 min to inactivate infectious virus. Cells were washed two times with PBS before secondary chemical inactivation of all of the surfaces by microdiffusion/nebulization to comply with biosafety regulations before extraction from the BSL3 laboratory, as described above.

Vitrified inactivated grids were transferred in liquid nitrogen to the cryocorrelative cooling stage (CMS196 stage; Linkam Scientific Instruments, UK) to hold samples at a stable temperature (−190 °C) during analysis. The cryo-stage was inserted into a Zeiss Axio Scope (Carl Zeiss, Germany) epifluorescence microscope that was used to visualize the frozen grids. Individual cells were inspected to determine overall cell morphology and subcellular localization of the fluorescent infection reporter.[23] Noninfected cell data sets were collected from mock-infected cultures, which displayed exclusively cytoplasmic fluorescence (Figure S2). Intermediate infection data sets were collected from infected cells displaying overall normal cell morphology but evident, albeit partial, nuclear localization of the infection reporter. Finally, late stages of infection data sets were collected from cells showing clear nuclear localization of the fluorescent reporter as well as alterations of the nuclear morphology and retraction of the cell cytoplasm (Figure S2). This cell classification is based on a detailed description of the temporal behavior of the infection reporter relative to virus inoculation time using fluorescence videomicroscopy previously reported in A549-ACE2 cells.[11,23] Subsequently, selected samples were transferred under cryogenic conditions to the Mistral beamline (ALBA light source) at the ALBA synchrotron. Tomographic data were collected at 520 eV, irradiating the samples for 1−2 s per projection. 520 eV is within the energy range in which water is transparent for X-rays and there is mostly absorbed by carbon, allowing the visualization of biological material. Three images per angle were acquired and combined. In a tomographic setup, images obtained at different sample orientations were computationally combined to produce a three-dimensional (3D) image, permitting the 3D representation of the subcellular ultrastructure of whole intact cells. A tilt series was acquired for each cell using an angular step of 1° on a 70° angular range with a Fresnel Zone plate (FZP) used to acquire the data having a 40 nm outermost zone width and effective pixel size of 13 nm.

Each transmission projection image of the tilt series was normalized using flat-field. This process also considers the possibly different exposure times as well as the slight decrease of the electron beam current during the acquisition. In order to increase the image quality, Wiener deconvolution considering the experimental impulse response of the optical system was applied to the normalized data.[44] Finally, the Napierian logarithm was used to reconstruct the linear absorption coefficient (LAC). The resulting stacks were then loaded into IMOD software[45] and the individual projections were aligned to the common tilt axis using the internal cellular structures as markers.[46] Subsequently, the aligned stacks were reconstructed with algebraic reconstruction techniques (ARTs).[47] Half-pitch spatial resolution was calculated following the Fourier Shell Correlation even/odd criterion defined by Cardone et al.[48] The spatial resolution obtained was 27.7 nm half pitch at 0.25 FSCe/o (Figure S3).

The visualization and segmentation of the volumes were carried out using Amira 3D software (ThermoFisher). The lengths of segmented structures were corrected for the in-depth elongation provoked by the missing wedge using the known diameter of the Au fiducials. Representative tomograms are publicly available through EMPIAR (data set ID 11688 and 11690).[49]

Mitochondrial morphological features and relative absorption contrast, as compared with mitochondria found in uninfected cells, were used to define each organelle as normal or abnormal, similar to a previous cryo-SXT study.[14] Normal mitochondria, which are predominant in noninfected samples, appear as rounded structures with well-defined cristae and an absorption contrast comparable with that of the cytoplasm. Mitochondrial cristae dilation is a hallmark of mitochondrial stress, and increased contrast may be derived from mitochondrial matrix condensation, another hallmark of mitochon-

https://doi.org/10.1021/acsnano.3c07265
ACS Nano XXXX, XXX, XXX−XXX

drial stress.[29] Mitochondria displaying dilated cristae and increased absorption contrast were considered abnormal.

ASSOCIATED CONTENT

Supporting Information

The Supporting Information is available free of charge at https://pubs.acs.org/doi/10.1021/acsnano.3c07265.

Z-stack series of Figure 2B showing spatial distribution of vimentin and dsRNA, representative images illustrating the usefulness of the fluorescent infection reporter to differentiate infected versus noninfected cells, and half-pitch spatial resolution calculated from the tomograms shown in Figure 5 (PDF)

All volume slices from segmented tomograms of control from Figure 5 (MP4)

All volume slices from segmented tomograms of intermediate infection stage from Figure 5 (MP4)

All volume slices from segmented tomograms of late infection stage from Figure 5 (MP4)

AUTHOR INFORMATION

Corresponding Authors

Eva Pereiro − *ALBA Synchrotron Light Source, 08290 Cerdanyola del Valles, Spain;* orcid.org/0000-0001-7626-5935; Email: epereiro@cells.es

Pablo Gastaminza − *Centro Nacional de Biotecnología, 28049 Madrid, Spain;* orcid.org/0000-0002-7873-5491; Email: pgastaminza@cnb.csic.es

Authors

Victoria Castro − *Centro Nacional de Biotecnología, 28049 Madrid, Spain;* orcid.org/0000-0001-9151-5138

Ana Joaquina Pérez-Berna − *ALBA Synchrotron Light Source, 08290 Cerdanyola del Valles, Spain*

Gema Calvo − *Centro Nacional de Biotecnología, 28049 Madrid, Spain*

Complete contact information is available at: https://pubs.acs.org/10.1021/acsnano.3c07265

Author Contributions

[⊥]Victoria Castro and Ana Joaquina Pérez-Berna contributed equally to this work.

Notes

The authors declare no competing financial interest.

ACKNOWLEDGMENTS

This study was funded by ALBA Synchrotron standard proposals 2022065884 and 2021024899, the Spanish National Research Council (grant number PIE-RD-COVID-19 ref E202020E079) and PID2020-115476RB-I00 funded by MCIN/AEI/10.13039/501100011033, and by "ERDF A way of making Europe" to the CNB-CSIC. This research work was also funded by the European Commission − NextGenerationEU (Regulation EU 2020/2094), through CSIC's Global Health Platform (PTI Salud Global). G.C. was initially supported by SAF2017-87846-R from the Spanish Ministry of Science, and V.C. was initially supported by PIE-RD-COVID-19. A.J.P.-B., G.C., V.C., E.P., and P.G. are part of the CoCID Consortium (cocid.eu), which has received funding from the European Union's Horizon 2020 research and innovation programme under grant agreement No. 1010171162. We acknowledge R. Molenkamp (Erasmus University Medical Center, Rotterdam, The Netherlands; participant of the EU-funded EVA-GLOBAL project, grant agreement 871029) for the SARS-CoV-2 strain NL/2020 virus, Ralf Bartenschlager lab for the SARS-CoV-2 reporter construct, L. Enjuanes (Department of Molecular and Cell Biology, CNB-CSIC) for the Vero-E6 cells, and Urtzi Garaigorta (Department of Molecular and Cell Biology, CNB-CSIC) for critically reading the manuscript. We acknowledge the outstanding technical support from the BSL3 laboratory, Advanced Microscopy, Electron Microscopy and Cryoelectron Microscopy Core facilities personnel at the CNB as well as the support of ALBA staff, in particular Andrea Sorrentino and Ricardo Valcarcel from the MISTRAL beamline.

REFERENCES

(1) Wu, F.; Zhao, S.; Yu, B.; Chen, Y.-M.; Wang, W.; Song, Z.-G.; Hu, Y.; Tao, Z.-W.; Tian, J.-H.; Pei, Y.-Y.; Yuan, M.-L.; Zhang, Y.-L.; Dai, F.-H.; Liu, Y.; Wang, Q.-M.; Zheng, J.-J.; Xu, L.; Holmes, E. C.; Zhang, Y.-Z. A New Coronavirus Associated with Human Respiratory Disease in China. *Nature* **2020**, *579* (7798), 265−269.

(2) Cui, J.; Li, F.; Shi, Z.-L. Origin and Evolution of Pathogenic Coronaviruses. *Nat. Rev. Microbiol* **2019**, *17* (3), 181−192.

(3) V'kovski, P.; Kratzel, A.; Steiner, S.; Stalder, H.; Thiel, V. Coronavirus Biology and Replication: Implications for SARS-CoV-2. *Nat. Rev. Microbiol* **2021**, *19* (3), 155−170.

(4) Jackson, C. B.; Farzan, M.; Chen, B.; Choe, H. Mechanisms of SARS-CoV-2 Entry into Cells. *Nat. Rev. Mol. Cell Biol.* **2022**, *23* (1), 3−20.

(5) Finkel, Y.; Mizrahi, O.; Nachshon, A.; Weingarten-Gabbay, S.; Morgenstern, D.; Yahalom-Ronen, Y.; Tamir, H.; Achdout, H.; Stein, D.; Israeli, O.; Beth-Din, A.; Melamed, S.; Weiss, S.; Israely, T.; Paran, N.; Schwartz, M.; Stern-Ginossar, N. The Coding Capacity of SARS-CoV-2. *Nature* **2021**, *589* (7840), 125−130.

(6) Sola, I.; Almazán, F.; Zúñiga, S.; Enjuanes, L. Continuous and Discontinuous RNA Synthesis in Coronaviruses. *Annual Review of Virology* **2015**, *2* (1), 265−288.

(7) Wang, Y.; Grunewald, M.; Perlman, S.; Maier, H. J.; Bickerton, E. Coronaviruses: An Updated Overview of Their Replication and Pathogenesis. *Methods in Molecular Biology* **2020**, *2203*, 1−29.

(8) Snijder, E. J.; Limpens, R. W. A. L.; de Wilde, A. H.; de Jong, A. W. M.; Zevenhoven-Dobbe, J. C.; Maier, H. J.; Faas, F. F. G. A.; Koster, A. J.; Bárcena, M. A Unifying Structural and Functional Model of the Coronavirus Replication Organelle: Tracking down RNA Synthesis. *PLoS Biol.* **2020**, *18* (6), e3000715.

(9) Ogando, N. S.; Dalebout, T. J.; Zevenhoven-Dobbe, J. C.; Limpens, R. W. A. L.; van der Meer, Y.; Caly, L.; Druce, J.; de Vries, J. J. C.; Kikkert, M.; Bárcena, M.; Sidorov, I.; Snijder, E. J. Y SARS-Coronavirus-2 Replication in Vero E6 Cells: Replication Kinetics, Rapid Adaptation and Cytopathology. *Journal of General Virology* **2020**, *101* (9), 925−940.

(10) Klein, S.; Cortese, M.; Winter, S. L.; Wachsmuth-Melm, M.; Neufeldt, C. J.; Cerikan, B.; Stanifer, M. L.; Boulant, S.; Bartenschlager, R.; Chlanda, P. SARS-CoV-2 Structure and Replication Characterized by in Situ Cryo-Electron Tomography. *Nat. Commun.* **2020**, *11* (1), 5885.

(11) Cortese, M.; Lee, J.-Y.; Cerikan, B.; Neufeldt, C. J.; Oorschot, V. M. J.; Köhrer, S.; Hennies, J.; Schieber, N. L.; Ronchi, P.; Mizzon, G.; Romero-Brey, I.; Santarella-Mellwig, R.; Schorb, M.; Boermel, M.; Mocaer, K.; Beckwith, M. S.; Templin, R. M.; Gross, V.; Pape, C.; Tischer, C.; Frankish, J.; Horvat, N. K.; Laketa, V.; Stanifer, M.; Boulant, S.; Ruggieri, A.; Chatel-Chaix, L.; Schwab, Y.; Bartenschlager, R. Integrative Imaging Reveals SARS-CoV-2-Induced Reshaping of Subcellular Morphologies. *Cell Host & Microbe* **2020**, *28* (6), 853−866.e5.

(12) Romero-Brey, I.; Merz, A.; Chiramel, A.; Lee, J.-Y.; Chlanda, P.; Haselman, U.; Santarella-Mellwig, R.; Habermann, A.; Hoppe, S.;

https://doi.org/10.1021/acsnano.3c07265
ACS Nano XXXX, XXX, XXX−XXX

Kallis, S.; Walther, P.; Antony, C.; Krijnse-Locker, J.; Bartenschlager, R. Three-Dimensional Architecture and Biogenesis of Membrane Structures Associated with Hepatitis C Virus Replication. *PLoS Pathog* **2012**, *8* (12), e1003056.
(13) Paul, D.; Hoppe, S.; Saher, G.; Krijnse-Locker, J.; Bartenschlager, R. Morphological and Biochemical Characterization of the Membranous Hepatitis C Virus Replication Compartment. *Journal of Virology* **2013**, *87* (19), 10612−10627.
(14) Pérez-Berná, A. J.; Rodríguez, M. J.; Chichón, F. J.; Friesland, M. F.; Sorrentino, A.; Carrascosa, J. L.; Pereiro, E.; Gastaminza, P. Structural Changes In Cells Imaged by Soft X-Ray Cryo-Tomography During Hepatitis C Virus Infection. *ACS Nano* **2016**, *10* (7), 6597−6611.
(15) Ivanov, A. V.; Bartosch, B.; Smirnova, O. A.; Isaguliants, M. G.; Kochetkov, S. N. HCV and Oxidative Stress in the Liver. *Viruses* **2013**, *5* (2), 439−469.
(16) Kounatidis, I.; Stanifer, M. L.; Phillips, M. A.; Paul-Gilloteaux, P.; Heiligenstein, X.; Wang, H.; Okolo, C. A.; Fish, T. M.; Spink, M. C.; Stuart, D. I.; Davis, I.; Boulant, S.; Grimes, J. M.; Dobbie, I. M.; Harkiolaki, M. 3D Correlative Cryo-Structured Illumination Fluorescence and Soft X-Ray Microscopy Elucidates Reovirus Intracellular Release Pathway. *Cell* **2020**, *182* (2), 515−530.e17.
(17) Uchida, M.; McDermott, G.; Wetzler, M.; Le Gros, M. A.; Myllys, M.; Knoechel, C.; Barron, A. E.; Larabell, C. A. Soft X-Ray Tomography of Phenotypic Switching and the Cellular Response to Antifungal Peptoids in *Candida Albicans*. *Proc. Natl. Acad. Sci. U.S.A.* **2009**, *106* (46), 19375−19380.
(18) Weiß, D.; Schneider, G.; Niemann, B.; Guttmann, P.; Rudolph, D.; Schmahl, G. Computed Tomography of Cryogenic Biological Specimens Based on X-Ray Microscopic Images. *Ultramicroscopy* **2000**, *84* (3), 185−197.
(19) Loconte, V.; Chen, J.-H.; Cortese, M.; Ekman, A.; Le Gros, M. A.; Larabell, C.; Bartenschlager, R.; Weinhardt, V. Using Soft X-Ray Tomography for Rapid Whole-Cell Quantitative Imaging of SARS-CoV-2-Infected Cells. *Cell Reports Methods* **2021**, *1* (7), 100117.
(20) Nahas, K. L.; Connor, V.; Scherer, K. M.; Kaminski, C. F.; Harkiolaki, M.; Crump, C. M.; Graham, S. C. Near-Native State Imaging by Cryo-Soft-X-Ray Tomography Reveals Remodelling of Multiple Cellular Organelles during HSV-1 Infection. *PLOS Pathogens* **2022**, *18* (7), e1010629.
(21) Garriga, D.; Chichón, F. J.; Calisto, B. M.; Ferrero, D. S.; Gastaminza, P.; Pereiro, E.; Pérez-Berna, A. J. Imaging of Virus-Infected Cells with Soft X-Ray Tomography. *Viruses* **2021**, *13* (11), 2109.
(22) Scherer, K. M.; Mascheroni, L.; Carnell, G. W.; Wunderlich, L. C. S.; Makarchuk, S.; Brockhoff, M.; Mela, I.; Fernandez-Villegas, A.; Barysevich, M.; Stewart, H.; Suau Sans, M.; George, C. L.; Lamb, J. R.; Kaminski-Schierle, G. S.; Heeney, J. L.; Kaminski, C. F. SARS-CoV-2 Nucleocapsid Protein Adheres to Replication Organelles before Viral Assembly at the Golgi/ERGIC and Lysosome-Mediated Egress. *Sci. Adv.* **2022**, *8* (1), eabl4895.
(23) Pahmeier, F.; Neufeldt, C. J.; Cerikan, B.; Prasad, V.; Pape, C.; Laketa, V.; Ruggieri, A.; Bartenschlager, R.; Cortese, M. A Versatile Reporter System To Monitor Virus-Infected Cells and Its Application to Dengue Virus and SARS-CoV-2. *Journal of Virology* **2021**, *95* (4), 16.
(24) Johnston, J. A.; Ward, C. L.; Kopito, R. R. Aggresomes: A Cellular Response to Misfolded Proteins. *J. Cell Biol.* **1998**, *143* (7), 1883−1898.
(25) Balis, J. U.; Bumgarner, S. D.; Paciga, J. E.; Paterson, J. F.; Shelley, S. A. Synthesis of Lung Surfactant-Associated Glycoproteins by A549 Cells: Description of an in Vitro Model for Human Type II Cell Dysfunction. *Experimental Lung Research* **1984**, *6* (3−4), 197−213.
(26) *MISTRAL: a transmission soft X-ray microscopy beamline for cryo nano-tomography of biological samples and magnetic domains imaging*. http://scripts.iucr.org/cgi-bin/paper?vv5105 (accessed 2023-07-25).
(27) Groen, J.; Conesa, J. J.; Valcárcel, R.; Pereiro, E. The Cellular Landscape by Cryo Soft X-Ray Tomography. *Biophys Rev.* **2019**, *11* (4), 611−619.
(28) Mendonça, L.; Howe, A.; Gilchrist, J. B.; Sheng, Y.; Sun, D.; Knight, M. L.; Zanetti-Domingues, L. C.; Bateman, B.; Krebs, A.-S.; Chen, L.; Radecke, J.; Li, V. D.; Ni, T.; Kounatidis, I.; Koronfel, M. A.; Szynkiewicz, M.; Harkiolaki, M.; Martin-Fernandez, M. L.; James, W.; Zhang, P. Correlative Multi-Scale Cryo-Imaging Unveils SARS-CoV-2 Assembly and Egress. *Nat. Commun.* **2021**, *12*, 4629.
(29) Zick, M.; Rabl, R.; Reichert, A. S. Cristae Formation—Linking Ultrastructure and Function of Mitochondria. *Biochimica et Biophysica Acta (BBA) - Molecular Cell Research* **2009**, *1793* (1), 5−19.
(30) Miller, B.; Silverstein, A.; Flores, M.; Cao, K.; Kumagai, H.; Mehta, H. H.; Yen, K.; Kim, S.-J.; Cohen, P. Host Mitochondrial Transcriptome Response to SARS-CoV-2 in Multiple Cell Models and Clinical Samples. *Sci. Rep* **2021**, *11* (1), 3.
(31) Groen, J.; Palanca, A.; Aires, A.; Conesa, J. J.; Maestro, D.; Rehbein, S.; Harkiolaki, M.; Villar, A. V.; Cortajarena, A. L.; Pereiro, E. Correlative 3D Cryo X-Ray Imaging Reveals Intracellular Location and Effect of Designed Antifibrotic Protein-Nanomaterial Hybrids. *Chem. Sci.* **2021**, *12* (45), 15090−15103.
(32) Perez-Berna, A.; Valcarcel, R.; Rodríguez, M.; Chichón, F.; Sorrentino, A.; Carrascosa, J.; Gastaminza, P.; Pereiro, E. The Dual-Axes for Soft X-Ray Cryo-Tomography Reveals Ultrastructural Alterations of the Host Cell during Hepatitis C Infection by Increasing the Isotropic Axial Resolution. *Microsc Microanal* **2017**, *23* (S1), 976−977.
(33) Zhang, Y.; Wen, Z.; Shi, X.; Liu, Y.-J.; Eriksson, J. E.; Jiu, Y. The Diverse Roles and Dynamic Rearrangement of Vimentin during Viral Infection. *Journal of Cell Science* **2021**, *134* (5), jcs250597.
(34) Wileman, T. Aggresomes and Autophagy Generate Sites for Virus Replication. *Science* **2006**, *312* (5775), 875−878.
(35) Cortese, M.; Goellner, S.; Acosta, E. G.; Neufeldt, C. J.; Oleksiuk, O.; Lampe, M.; Haselmann, U.; Funaya, C.; Schieber, N.; Ronchi, P.; Schorb, M.; Pruunsild, P.; Schwab, Y.; Chatel-Chaix, L.; Ruggieri, A.; Bartenschlager, R. Ultrastructural Characterization of Zika Virus Replication Factories. *Cell Reports* **2017**, *18* (9), 2113−2123.
(36) Wang, L.; Moreira, E. A.; Kempf, G.; Miyake, Y.; Oliveira Esteves, B. I.; Fahmi, A.; Schaefer, J. V.; Dreier, B.; Yamauchi, Y.; Alves, M. P.; Plückthun, A.; Matthias, P. Disrupting the HDAC6-Ubiquitin Interaction Impairs Infection by Influenza and Zika Virus and Cellular Stress Pathways. *Cell Reports* **2022**, *39* (4), 110736.
(37) Zhang, Y.; Zhao, S.; Li, Y.; Feng, F.; Li, M.; Xue, Y.; Cui, J.; Xu, T.; Jin, X.; Jiu, Y. Host Cytoskeletal Vimentin Serves as a Structural Organizer and an RNA-Binding Protein Regulator to Facilitate Zika Viral Replication. *Proc. Natl. Acad. Sci. U. S. A.* **2022**, *119* (8), e2113909119.
(38) Johnston, H. E.; Samant, R. S. Alternative Systems for Misfolded Protein Clearance: Life beyond the Proteasome. *FEBS Journal* **2021**, *288* (15), 4464−4487.
(39) Kaganovich, D.; Kopito, R.; Frydman, J. Misfolded Proteins Partition between Two Distinct Quality Control Compartments. *Nature* **2008**, *454* (7208), 1088−1095.
(40) Ogrodnik, M.; Salmonowicz, H.; Brown, R.; Turkowska, J.; Średniawa, W.; Pattabiraman, S.; Amen, T.; Abraham, A.; Eichler, N.; Lyakhovetsky, R.; Kaganovich, D. Dynamic JUNQ Inclusion Bodies Are Asymmetrically Inherited in Mammalian Cell Lines through the Asymmetric Partitioning of Vimentin. *Proc. Natl. Acad. Sci. U. S. A.* **2014**, *111* (22), 8049−8054.
(41) Jimenez-Aleman, G. H.; Castro, V.; Londaitsbehere, A.; Gutierrez-Rodríguez, M.; Garaigorta, U.; Solano, R.; Gastaminza, P. SARS-CoV-2 Fears Green: The Chlorophyll Catabolite Pheophorbide A Is a Potent Antiviral. *Pharmaceuticals (Basel)* **2021**, *14* (10), 1048.
(42) REED, L. J.; MUENCH, H. A SIMPLE METHOD OF ESTIMATING FIFTY PER CENT ENDPOINTS12. *American Journal of Epidemiology* **1938**, *27* (3), 493−497.
(43) Schindelin, J.; Arganda-Carreras, I.; Frise, E.; Kaynig, V.; Longair, M.; Pietzsch, T.; Preibisch, S.; Rueden, C.; Saalfeld, S.;

https://doi.org/10.1021/acsnano.3c07265
ACS Nano XXXX, XXX, XXX−XXX

Schmid, B.; Tinevez, J.-Y.; White, D. J.; Hartenstein, V.; Eliceiri, K.; Tomancak, P.; Cardona, A. Fiji: An Open-Source Platform for Biological-Image Analysis. *Nat. Methods* **2012**, *9* (7), 676−682.
(44) Otón, J.; Pereiro, E.; Pérez-Berná, A. J.; Millach, L.; Sorzano, C. O. S.; Marabini, R.; Carazo, J. M. Characterization of Transfer Function, Resolution and Depth of Field of a Soft X-Ray Microscope Applied to Tomography Enhancement by Wiener Deconvolution. *Biomed Opt Express* **2016**, *7* (12), 5092−5103.
(45) Kremer, J. R.; Mastronarde, D. N.; McIntosh, J. R. Computer Visualization of Three-Dimensional Image Data Using IMOD. *J. Struct. Biol.* **1996**, *116* (1), 71−76.
(46) Kremer, J. R.; Mastronarde, D. N.; McIntosh, J. R. Computer Visualization of Three-Dimensional Image Data Using IMOD. *J. Struct. Biol.* **1996**, *116* (1), 71−76.
(47) Gordon, R.; Bender, R.; Herman, G. T. Algebraic Reconstruction Techniques (ART) for Three-Dimensional Electron Microscopy and X-Ray Photography. *J. Theor. Biol.* **1970**, *29* (3), 471−481.
(48) Cardone, G.; Grünewald, K.; Steven, A. C. A Resolution Criterion for Electron Tomography Based on Cross-Validation. *J. Struct. Biol.* **2005**, *151* (2), 117−129.
(49) Iudin, A.; Korir, P. K.; Somasundharam, S.; Weyand, S.; Cattavitello, C.; Fonseca, N.; Salih, O.; Kleywegt, G. J.; Patwardhan, A. EMPIAR: The Electron Microscopy Public Image Archive. *Nucleic Acids Res.* **2023**, *51* (D1), D1503−D1511.

https://doi.org/10.1021/acsnano.3c07265
ACS Nano XXXX, XXX, XXX−XXX